Enhanced Automatic-Power-Decoupling Control Method for Single-Phase AC-to-DC Converters

***Abstract*—Existing control schemes for a single-phase ac-to-dc converter with active power-decoupling function typically involve a dedicated power-decoupling controller. However, due to the highly coupled and nonlinear nature of the single-phase system, the design of the power-decoupling controller based on the conventional linear control techniques is cumbersome, and the control structure is complicated. Additionally, with the power-decoupling control, it is generally difficult to achieve satisfied dynamic responses and robust circuit operation. Following a recently proposed automatic-power-decoupling control scheme, this paper proposes a nonlinear control method that can achieve enhanced dynamic responses and strong disturbance rejection performance without the need for a dedicated power-decoupling controller. The proposed controller has a simple structure, of which the design is straightforward. In addition, the control method is generally applicable to single-phase ac-to-dc systems with active power-decoupling function. Simulation and experimental results validate the feasibility of the proposed control method on a two-switch buck-boost PFC rectifier prototype.**

***Index Terms*—Automatic power decoupling control, single-phase ac-to-dc converters, power decoupling.**

I. Introduction

In single-phase ac-to-dc power conversion systems, a ripple power at double line frequency is inherently injected from the ac side to the dc side [1]–[3]. To maintain a stable dc side voltage without low-frequency fluctuation, the ripple power must be properly buffered using an energy storage. The conventional passive power-buffering method, e.g., by directly paralleling an electrolytic capacitor (E-cap) to the dc side, is easy to apply. Due to the requirement of using E-caps, such a method has the well-known issues of degrading the system's performance on reliability, cost and power density [4]–[6]. The active power-buffering (or active

power-decoupling) methods, on the other hand, can effectively reduce the capacitance needed for ripple-power buffering [7]–[10]. It offers the opportunity to employ non-electrolytic capacitor (non-E-caps) with long lifetime (e.g. film capacitors) in the circuit in lieu of E-caps. The basic idea with these methods is to employ a power-decoupling circuitry to divert the ripple power into an extra energy storage component, e.g., a capacitor that has a large voltage fluctuation, such that only a small capacitance is required to handle the ripple power. It has been shown in [11]–[17] that through systematic component integration, it is possible to achieve active power decoupling of the single-phase ac-to-dc system without adding any extra passive/active devices and circuit. Thus, low system's cost, high power density, and high energy efficiency can be achieved.

On the other hand, the performance of such single-phase systems with active power-decoupling function also depends on the controller design. A dual voltage control strategy is often adopted for the control, where one loop is responsible for direct ac-side power control, and the other loop is for direct ripple-power-decoupling control [18]. The need for direct ripple-power-decoupling control inherently leads to three major issues: (i) high computational and/or control complexity that mandates expensive controller, (ii) inaccuracy or incapability of ripple-power compensation, especially during transient and disturbed (e.g. with unknown frequencies) situations, and (iii) difficulty in system response prediction and effective compensator designs. Due to these limitations, a low-cost and high-performance single-phase system with power decoupling function is still unavailable. Advancement in this aspect has recently been reported in [19], [20], which describe a new control strategy that directly controls the ac and the dc side power without the need of a dedicated power-decoupling controller. With this strategy, the ripple power will be automatically transferred to the power-buffering capacitor without any control effort. However, as will be discussed in Section II, the existing control structure of an automatic-power-decoupling control and its design is still complicated. Moreover, the closed-loop system is still susceptible to various disturbances, due to the internal coupling of the ac, the dc and the ripple powers within the system.

In this paper, an enhanced automatic-power-decoupling control is proposed. The proposed controller is easy to apply, and its design methodology is simple. In addition, the closed-loop system with the proposed

control exhibits improved dynamic responses and strong disturbance rejection performance. In Section II, an analysis of the existing active power decoupling control strategies based on a generic three-port circuit model is provided. In Section III, the basic principles of the proposed enhanced automatic-power-decoupling control are explained. The control is applied to a recently proposed two-switch buck-boost PFC rectifier [19] as an illustrative example. Finally, in Section V, the feasibility and strengths of the proposed control over existing control methods are examined by simulations and experiments, including (i) steady-state tests with ideal/peak-clipped ac input voltage, (ii) transient tests with a step change of the input voltage, the reference of the output voltage and the load, and (iii) start-up and shut-down tests.

II. Control Analysis of Single-Phase System with Active Power-decoupling Function

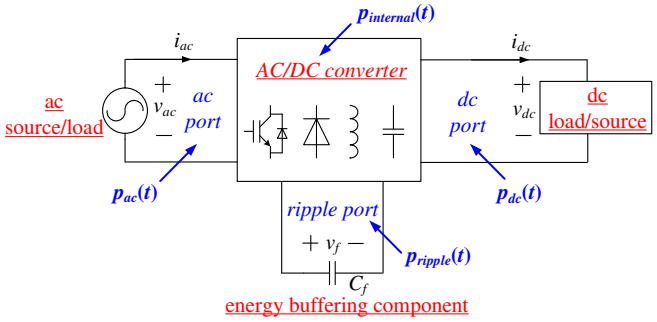

Fig. 1. A generic three-port model for a single-phase system with active power-decoupling function.

Fig. 1 illustrates a generic three-port model for a single-phase system with active power-decoupling function, where the ac- and dc- ports are respectively interfaced to an ac source/load and a dc load/source, and the ripple-port is connected to an energy storage device, e.g. a capacitor C_f. The basic function of the system is to achieve (i) power conversion between the ac and the dc ports, and (ii) ripple-power buffering through the ripple port, such that the dc port voltage v_{dc} is constant without low-frequency voltage fluctuation.

A. *Control Strategies*

According to energy conservation principle and with reference to Fig. 1, one yields

$$p_{ac}(t) - p_f(t) - p_{dc}(t) - p_{internal}(t) = 0, \tag{1}$$

where p_{ac}, p_{dc}, and p_f are respectively the instantaneous powers at the ac, the dc, and the ripple ports, and they are controllable through the switching action of the internal active switches. $p_{internal}$ represents all the power losses and small reactive power (e.g. produced by the internal inductors and/or capacitors) from within the system.

Equation (1) indicates that the power at *any* port is inherently determined by that of the other two. Therefore, only two out of the three port-power terms need to be controlled. Correspondingly, there are three possible control strategies for regulating the three-port system:

Strategy A: direct control of ac- and ripple-port power;

Strategy B: direct control of dc- and ripple-port power;

Strategy C: direct control of ac- and dc-port power.

Since *Strategy A* and *Strategy B* involve direct control of the ripple-port power, they are referred to as direct-power-decoupling (DPD) control hereinafter. On the other hand, no dedicated ripple-port power control is required with *Strategy C*. Therefore, *Strategy C* is referred to as automatic-power-decoupling (APD) control hereinafter.

Theoretically, the three control strategies are equivalent and can achieve the same steady-state and transient performances if the reference at the associated ports can be precisely generated and tracked. Fig. 2(a) and (b) depict the typical control block diagrams for DPD (with *Strategy A*) and APD (with *Strategy C*) control, respectively. In Fig. 2 (a), p_{ac} and p_f are controlled via the control of i_{ac} and v_f through the control inputs d_g and d_f, respectively, where d_g and d_f are the duty cycles of the active switches of the three-port system. The reference of i_{ac}, i.e., i_{ac}^*, is generated by an outer voltage loop, where the dc portion of v_{dc}, i.e., v_{dc0}, is controlled. The reference of v_f can be generated either by an open-loop calculation or a closed-loop control of v_{dcr} (i.e., the ripple portion of v_{dc}). Note that other state variables can also be used to achieve the required port-power control. For example, the current through C_f is another common selection for regulating p_f, as shown in Fig. 2(a).

On the other hand, with *Strategy C*, p_{ac} and p_{dc} are directly controlled as shown in Fig. 2(b). The control of i_{ac} is similar to that shown in Fig. 2(a), except that i_{ac}^* is generated by an outer voltage loop regulating the dc portion of v_f, i.e., v_{f0}. Also, a single-loop control is employed for controlling v_{dc} (through the control input d_v) without an outer reference-generation loop, since the reference of v_{dc} is typically predetermined.

B. Reference Generation at the Ripple-Port

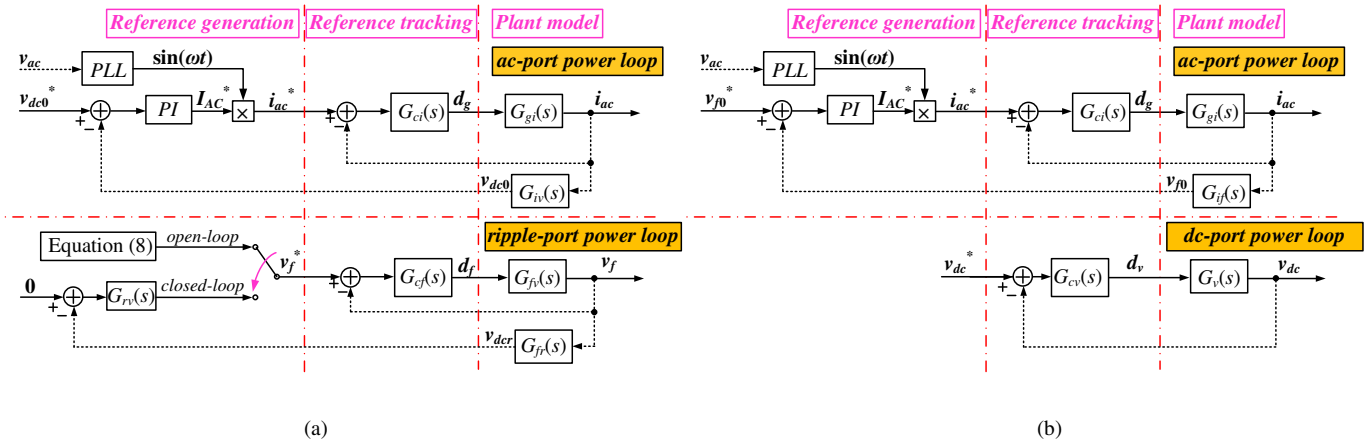

Fig. 2. Typical control block diagrams of (a) direct-power-decoupling control (*Strategy A*) and (b) automatic-power-decoupling control (*Strategy C*).

As mentioned, there are two methods to generate the reference at the ripple port: open-loop calculation method and closed-loop feedback control method. The open-loop method is based on instantaneous power analysis. According to (1), the ripple-port power which needs to be buffered can be expressed as

$$p_f(t) = p_{ac}(t) - p_{dc}(t) - p_{internal}(t). \tag{2}$$

Ideally, if (i) the power losses and reactive power within the system are zero, i.e., $p_{internal} = 0$, and (ii) the ac-port voltage and current waveforms are pure sinusoidal, i.e.,

$$v_{ac}(t) = V_{AC}\sin(\omega t), \tag{3}$$

$$i_{ac}(t) = I_{AC}\sin(\omega t + \theta), \tag{4}$$

where V_{AC} and I_{AC} are the magnitude of the ac voltage and current, respectively, and θ is the power angle.Then, p_{ac} can be determined as

$$p_{ac}(t) = v_{ac}(t)i_{ac}(t) = \frac{V_{AC}I_{AC}}{2}\cos\theta - \frac{V_{AC}I_{AC}}{2}\cos(2\omega t + \theta). \tag{5}$$

Clearly, a double-line-frequency ripple power is injected from the ac port besides a dc power component. By assuming that p_{dc} is constant and according to (2), one yields

$$p_{dc}(t) = \frac{V_{AC} I_{AC}}{2} \cos\theta, \tag{6}$$

$$p_f(t) = -\frac{V_{AC} I_{AC}}{2} \cos(2\omega t + \theta). \tag{7}$$

Based on (7), the voltage reference at the ripple-port, i.e., v_f^*, can be directly calculated as [17]

$$v_f^*(t) = \pm\sqrt{K - \frac{V_{AC} I_{AC}}{2\omega C_f} \sin(2\omega t + \theta)}, \tag{8}$$

where K is a constant that determines the dc value of v_f^* and the polarity is dependent on the specific circuit topology.

It should be emphasized that the system parameters (e.g. C_f) cannot be easily controlled in a mass production due to manufacturing tolerance and aging effect. In addition, a practical system is always non-ideal (e.g. v_{ac} might contain background harmonics, p_{dc} might be time-varying according to the loading conditions, and $p_{internal} \neq 0$ due to the power losses). The true ripple power that needs to be buffered can be more complex than (7). Accurate prediction of p_f is hence impractical and even impossible. Due to the above reasons, DPD control based on open-loop reference generation is known to be less effective for achieving satisfactory power-decoupling performance [9], [17], [21].

On the other hand, closed-loop reference-generation methods are often employed to improve the accuracy of the ripple-port reference generation. As shown in Fig. 2(a), the reference is generated through a feedback mechanism such that $v_{dcr} = 0$ (i.e., v_{dc} is constant). The closed-loop reference-generation methods are more effective than the open-loop solution in the sense that (i) the exact values of the system parameters are not needed, and (ii) the reference generation is more adaptive to internal and external disturbances. Nevertheless, precise generation of v_f^* is still challenging. On the one hand, v_f^* is directly dependent on the outer loop compensator (i.e., $G_{rv}(s)$ in Fig. 2 (a)), which is a design choice [17]. For instance, *multiple-proportional-resonant* (MPR) compensators (or repetitive controllers) with resonant poles at multiples of line frequency

are often chosen for G_{rv} (s). However, the number of resonant poles that can be implemented is practically limited by the computational capability of the digital controller used in the design. On the other hand, the gain of MPR compensators is only significant at discrete frequencies (i.e., multiples of line frequency). In the presence of a general form of disturbances (e.g. disturbances with unknown frequencies, transient disturbances during voltage sag/swell, a step change of the load), MPR compensators will be less effective for generating a proper reference signal for v_f^*.

In contrast to DPD control, the APD control does not require reference generation at the ripple port. For this reason, one may conclude that:

(i) the structure of APD control is simpler than the DPD control, due to the elimination of a dedicated reference generation loop, and

(ii) the performance of APD control is potentially more robust than that with the DPD control. This is because v_{dc} is directly controlled with APD method, while it is indirectly controlled by the ac and the ripple port with DPD method, where precise reference generation at the ripple port is difficult.

C. *System Modeling and Compensator Designs*

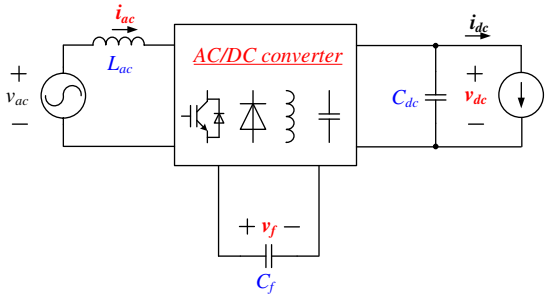

Fig. 3. Three-port configuration with L_{ac} and C_{dc} at the ac and the dc port.

Besides reference generation, accurate reference tracking is also crucial to the performance of the single-phase system. Consider the three-port configuration illustrated in Fig. 3, where the ac and the dc port are respectively connected to an ac voltage source v_{ac} and a dc sink i_{dc} through an interfacing inductor L_{ac} and a capacitor C_{dc}. The state-space equation of the three-port system can be expressed as

$$\begin{bmatrix} L_{ac} & 0 & 0 \\ 0 & C_{dc} & 0 \\ 0 & 0 & C_f \end{bmatrix} \begin{bmatrix} \dot{i}_{ac} \\ \dot{v}_{dc} \\ \dot{v}_f \end{bmatrix} = \begin{bmatrix} A_{11} & A_{12} & A_{13} \\ A_{21} & A_{22} & A_{23} \\ A_{31} & A_{32} & A_{33} \end{bmatrix} \begin{bmatrix} i_{ac} \\ v_{dc} \\ v_f \end{bmatrix} + \begin{bmatrix} B_{11} & B_{12} \\ B_{21} & B_{22} \\ B_{31} & B_{32} \end{bmatrix} \begin{bmatrix} v_{ac} \\ i_{dc} \end{bmatrix} \tag{9}$$

which can be written in a simple form as

$$\boldsymbol{K}\dot{\boldsymbol{X}} = \boldsymbol{A}\boldsymbol{X} + \boldsymbol{B}\boldsymbol{U}. \tag{10}$$

In (10), the topology-specific matrixes $\boldsymbol{A}$ and $\boldsymbol{B}$ represent the effect of the control inputs (e.g. d_g, d_f and/or d_v), and are not necessarily diagonal matrixes. Therefore, the three-port system illustrated in Fig. 3 can be highly coupled (between the state variables and between the control inputs) and nonlinear (due to the product operation of the matrix $\boldsymbol{A}$, $\boldsymbol{B}$ with $\boldsymbol{X}$). The same conclusion also holds for other three-port configurations.

To facilitate the compensator design, the coupled and non-linear three-port system is often considered as two decoupled subsystems [17], [18]. For instance, (11) and (12) are often adopted to approximate (9) for compensator design in the DPD control (*Strategy A*).

$$\begin{bmatrix} L & 0 \\ 0 & C_{dc} \end{bmatrix} \begin{bmatrix} \dot{i}_{ac} \\ \dot{v}_{dc0} \end{bmatrix} = \begin{bmatrix} A_{11}' & A_{12}' \\ A_{21}' & A_{22}' \end{bmatrix} \begin{bmatrix} i_{ac} \\ v_{dc0} \end{bmatrix} + \begin{bmatrix} B_{11}' & 0 \\ B_{21}' & 0 \end{bmatrix} \begin{bmatrix} v_{ac} \\ 0 \end{bmatrix}, \tag{11}$$

$$\begin{bmatrix} C_f & 0 \\ 0 & C_{dc} \end{bmatrix} \begin{bmatrix} \dot{v}_f \\ \dot{v}_{dcr} \end{bmatrix} = \begin{bmatrix} A_{11}'' & A_{12}'' \\ A_{21}'' & A_{22}'' \end{bmatrix} \begin{bmatrix} v_f \\ v_{dcr} \end{bmatrix} + \begin{bmatrix} B_{11}'' & 0 \\ B_{21}'' & 0 \end{bmatrix} \begin{bmatrix} v_{ac} \\ 0 \end{bmatrix}, \tag{12}$$

where the dynamics of the ac port (i.e., i_{ac}) is only related to v_{dc0}, and the dynamics of ripple port (i.e., v_f) is only related to v_{dcr}. Small-signal analysis is then carried out over the approximated circuit model, and the plant transfer functions (e.g. $G_{gi}(s)$, $G_{iv}(s)$, $G_{fv}(s)$, and $G_{fr}(s)$ in Fig. 2 (a)) are obtained. Based on specific bandwidth and stability requirements, the associated inner-loop compensators (e.g. $G_{ci}(s)$ and $G_{cf}(s)$ in Fig. 2(a)) are then designed. A similar system modeling and compensator design approach also apply to existing APD control (e.g. for designing $G_{ci}(s)$ and $G_{cv}(s)$ in Fig. 2 (b)).

One major limitation with the above compensator design approach is that the system is susceptible to disturbances since the inherent coupling among the three ports are neglected based on the model of (11) and (12). To ensure good reference tracking and effective disturbance rejection, MPR (or repetitive) compensators are employed as the inner loop compensators in the existing control solutions. Similar to the

outer loop MPR compensator design for ripple-port reference generation in Fig. 2(a), the effectiveness of the MPR controllers for reference tracking are determined by the computational capability of the digital controller used and by the nature of the system disturbances.

III. Proposed Enhanced Automatic Power-Decoupling Control

In this section, the proposed enhanced control method based on APD control (*Strategy C*) such that (i) no MPR (or repetitive) compensators are utilized, and (ii) a robust and intuitive controller design can be easily attained, is described. The proposed control method is general and applicable to any single-phase system that has an active power-decoupling function.

A. *Basic Principle*

As mentioned in Section II, v_f is not a direct control variable with the control *Strategy C*. Additionally, the dynamics of v_f is automatically determined by that of i_{ac} and v_{dc}. Therefore, v_f is redundant and can be disregarded during the system modeling process. In particular, (9) can be simplified as

$$\begin{bmatrix} L_{ac} & 0 \\ 0 & C_{dc} \end{bmatrix} \begin{bmatrix} \dot{i}_{ac} \\ \dot{v}_{dc} \end{bmatrix} = \begin{bmatrix} A_{11} & A_{12} & A_{13} \\ A_{21} & A_{22} & A_{23} \end{bmatrix} \begin{bmatrix} i_{ac} \\ v_{dc} \\ v_f \end{bmatrix} + \begin{bmatrix} B_{11} & B_{12} \\ B_{21} & B_{22} \end{bmatrix} \begin{bmatrix} v_{ac} \\ i_{dc} \end{bmatrix}, \tag{13}$$

where only the dynamics at the ac port (i.e., i_{ac}) and that at the dc port (i.e., v_{dc}), are described. Unlike the existing system model represented by (11) and (12), the model represented by (13) retains all the coupling factors and nonlinearities of the system and is a more accurate representation of the three-port system.

Notice that (13) can be re-arranged as

$$\begin{bmatrix} L_{ac} & 0 \\ 0 & C_{dc} \end{bmatrix} \begin{bmatrix} \dot{i}_{ac} \\ \dot{v}_{dc} \end{bmatrix} = \begin{bmatrix} A_{11} & 0 \\ 0 & A_{22} \end{bmatrix} \begin{bmatrix} i_{ac} \\ v_{dc} \end{bmatrix} + \begin{bmatrix} u_A \\ u_B \end{bmatrix}, \tag{14}$$

where

$$\begin{bmatrix} u_A \\ u_B \end{bmatrix} = \begin{bmatrix} 0 & A_{12} & A_{13} \\ A_{21} & 0 & A_{23} \end{bmatrix} \begin{bmatrix} i_{ac} \\ v_{dc} \\ v_f \end{bmatrix} + \begin{bmatrix} B_{11} & B_{12} \\ B_{21} & B_{22} \end{bmatrix} \begin{bmatrix} v_{ac} \\ i_{dc} \end{bmatrix}. \tag{15}$$

Equation (14) describes two decoupled, first-order linear systems, if u_A and u_B are treated as two new and mutually independent control inputs for regulating i_{ac} and v_{dc}, respectively. As the system model now becomes two first-order subsystems, the design of the associated compensator is easy and straightforward. Simple *proportional-integral (PI)* compensator or even *proportional* (*P*) compensator can be utilized to achieve the desired reference tracking performance. Additionally, since the dynamics at the ac and the dc port are now decoupled, the system compensators can be individually designed and the dynamic response of the system can be easily predicted.

In this paper, the system controller that is designed based on the circuit modeling approach given by (14) is referred to as enhanced automatic-power-decoupling (E-APD) control.

B. Controller Design Example for a Two-Switch Buck-Boost PFC Rectifier

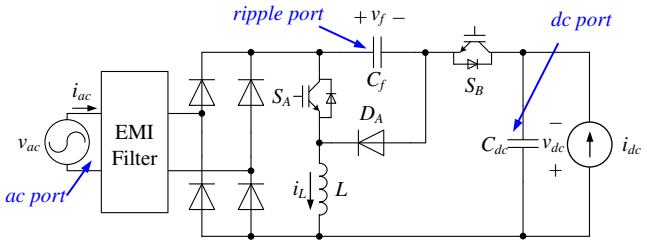

Fig. 4. Circuit topologies of a two-switch buck-boost PFC rectifier [19].

In this subsection, the design of the proposed controller is demonstrated on a recently reported two-switch buck-boost PFC rectifier (See Fig. 4) [19]. The rectifier incorporates only two active switches S_A and S_B, one inductor L (for controlling the power at the ac port), one small power-buffering capacitor C_f (for power decoupling at the ripple port) and one small output capacitor C_{dc} (for filtering the switching ripples at the dc port). The circuit can be perceived as an integration of a conventional buck-boost PFC rectifier and an active power-decoupling circuit. It is an interesting circuit topology for control design illustration as it contains the minimum number of active switches used among all existing single-phase solutions that have a power-decoupling function.

1) System Modeling

The operating states of the rectifier are illustrated in Fig. 5, where a continuous-conduction-mode of operation is assumed, and the effect of the front-end EMI filter is neglected. The diode D_r in Fig. 5 is an equivalent representation of the front-end diode bridge in Fig. 4. The rectifier has four operating states. *State* 1 and *State* 2 are identical to that of the conventional buck-boost converter, and C_f is not involved in the circuit operation. In *State* 3 and *State* 4, C_f is a part of the power flow path and can either store (i.e., C_f is charged by the inductor current i_L in *State* 3) or release (i.e., C_f is discharged by i_L in *State* 4) energy. Therefore, active power decoupling can be achieved by properly controlling the duration of *State* 3 and *State* 4.

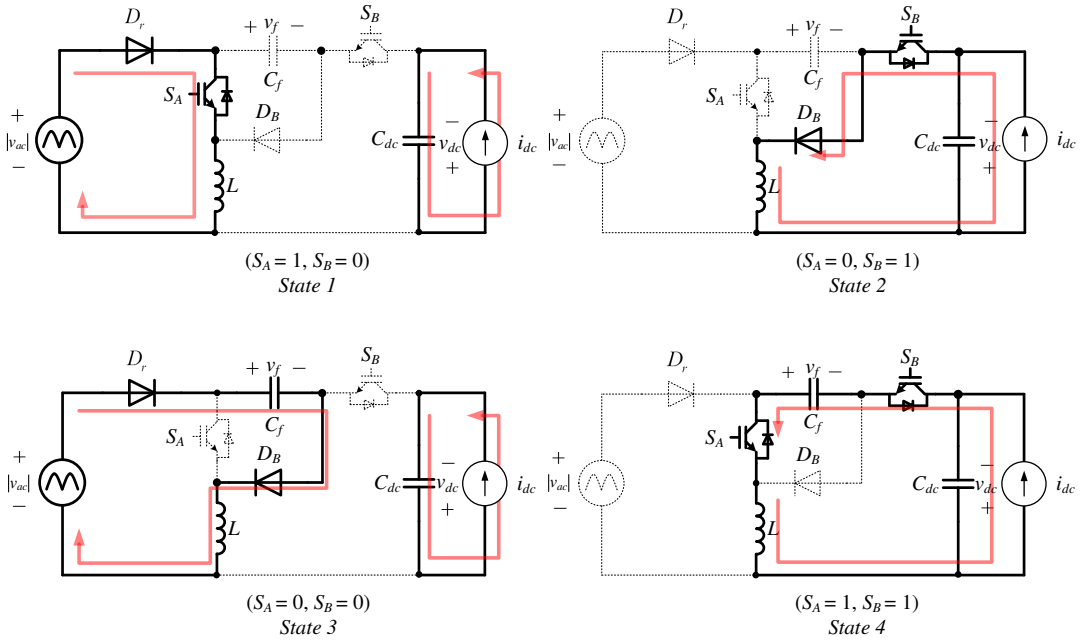

Fig. 5. Equivalent circuits of the two-switch buck-boost PFC rectifier during State 1–State 4.

According to Fig. 5, the state-space-averaged equations of the rectifier over one switching period T_s can be expressed as [19]

$$\begin{bmatrix} L & 0 & 0 \\ 0 & C_{dc} & 0 \\ 0 & 0 & C_f \end{bmatrix} \begin{bmatrix} \dot{i}_L \\ \dot{v}_{dc} \\ \dot{v}_f \end{bmatrix} = \begin{bmatrix} 0 & -d_B & d_A + d_B - 1 \\ d_B & 0 & 0 \\ 1 - d_A - d_B & 0 & 0 \end{bmatrix} \begin{bmatrix} i_L \\ v_{dc} \\ v_f \end{bmatrix} + \begin{bmatrix} 1 - d_B & 0 \\ 0 & -1 \end{bmatrix} \begin{bmatrix} |v_{ac}| \\ i_{dc} \end{bmatrix} \tag{16}$$

where d_A and d_B are the duty cycles of the switches S_A and S_B, respectively. As compared to the state-space equation (9), in (16), the inductor current i_L, instead of the ac-port current i_{ac}, is selected as the ac-port state

variable. The reason is that the ac port is not directly connected to an inductor as that shown in Fig. 3, and the measurement of the averaged ac-port current requires additional design efforts. Notice that i_L can be used to control the averaged ac port current/power. Hence, i_L is chosen as the ac port state variable for control convenience. In particular, the averaged inductor current i_L over T_s can be derived as

$$i_L = |i_{ac}| + i_{dc}. \tag{17}$$

One operating constraint of the rectifier is

$$v_{dc} \le v_f - |v_{ac}|, \tag{18}$$

Therefore, the safe turn on/off of the diodes D_r and D_B during the operation can be ensured.

As mentioned, the dynamics of v_f is redundant with E-APD control. Thus, (16) can be simplified as

$$\begin{bmatrix} L & 0 \\ 0 & C_{dc} \end{bmatrix} \begin{bmatrix} \dot{i}_L \\ \dot{v}_{dc} \end{bmatrix} = \begin{bmatrix} 0 & -d_B & d_A + d_B - 1 \\ d_B & 0 & 0 \end{bmatrix} \begin{bmatrix} i_L \\ v_{dc} \\ v_f \end{bmatrix} + \begin{bmatrix} 1-d_B & 0 \\ 0 & -1 \end{bmatrix} \begin{bmatrix} |v_{ac}| \\ i_{dc} \end{bmatrix}. \tag{19}$$

With reference to (14) and considering a fixed resistive load R_o that is connected to the output, i.e.,

$$i_{dc} = \frac{v_{dc}}{R_o}, \tag{20}$$

then (19) can be rearranged as

$$\begin{bmatrix} L & 0 \\ 0 & C_{dc} \end{bmatrix} \begin{bmatrix} \dot{i}_L \\ \dot{v}_{dc} \end{bmatrix} = \begin{bmatrix} 0 & 0 \\ 0 & -\dfrac{1}{R_o} \end{bmatrix} \begin{bmatrix} i_L \\ v_{dc} \end{bmatrix} + \begin{bmatrix} u_A \\ u_B \end{bmatrix}, \tag{21}$$

where the two new control inputs, u_A and u_B, are

$$\begin{bmatrix} u_A \\ u_B \end{bmatrix} = \begin{bmatrix} 0 & -d_B & d_A + d_B - 1 \\ d_B & 0 & 0 \end{bmatrix} \begin{bmatrix} i_L \\ v_{dc} \\ v_f \end{bmatrix} + \begin{bmatrix} 1-d_B & 0 \\ 0 & 0 \end{bmatrix} \begin{bmatrix} |v_{ac}| \\ 0 \end{bmatrix}. \tag{22}$$

Solution of (22) yields

$$\begin{bmatrix} d_A \\ d_B \end{bmatrix} = \begin{bmatrix} \left[u_A - \left(|v_{ac}| - v_f \right) + d_B \left(|v_{ac}| - v_f + v_{dc} \right) \right] / v_f \\ u_B / i_L \end{bmatrix}. \tag{23}$$

Equation (21) describes two decoupled, first-order and linear systems, where i_L and v_{dc} can be individually controlled by u_A and u_B. In many cases where the load is constantly changing or is not necessarily resistive,

the system model described by (21) is invalid. In these scenarios, feedback linearization based on i_{dc} may be directly employed, and the new control inputs can be selected as

$$\begin{bmatrix} u_A \\ u_B' \end{bmatrix} = \begin{bmatrix} 0 & -d_B & d_A + d_B - 1 \\ d_B & 0 & 0 \end{bmatrix} \begin{bmatrix} i_L \\ v_{dc} \\ v_f \end{bmatrix} + \begin{bmatrix} 1 - d_B & 0 \\ 0 & -1 \end{bmatrix} \begin{bmatrix} |v_{ac}| \\ i_{dc} \end{bmatrix}. \tag{24}$$

Thus,

$$\begin{bmatrix} d_A \\ d_B \end{bmatrix} = \begin{bmatrix} \left[u_A - \left(|v_{ac}| - v_f \right) + d_B \left(|v_{ac}| - v_f + v_{dc} \right) \right] / v_f \\ \left(u_B' + i_{dc} \right) / i_L \end{bmatrix}. \tag{25}$$

Combination of (19) and (25) leads to

$$\begin{bmatrix} L & 0 \\ 0 & C_{dc} \end{bmatrix} \begin{bmatrix} \dot{i}_L \\ \dot{v}_{dc} \end{bmatrix} = \begin{bmatrix} 0 & 0 \\ 0 & 0 \end{bmatrix} \begin{bmatrix} i_L \\ v_{dc} \end{bmatrix} + \begin{bmatrix} u_A \\ u_B' \end{bmatrix}, \tag{26}$$

which describes another first-order linear system controlled by u_A and u_B'. Compared to (23), one additional current sensor for measuring i_{dc} is needed in (25) for obtaining d_A and d_B. Since the focus of this subsection is to demonstrate how to decouple the dynamics of the three-port system and how to design the system compensators, only a fixed resistive load of R_o is considered here.

2) System Compensators Design

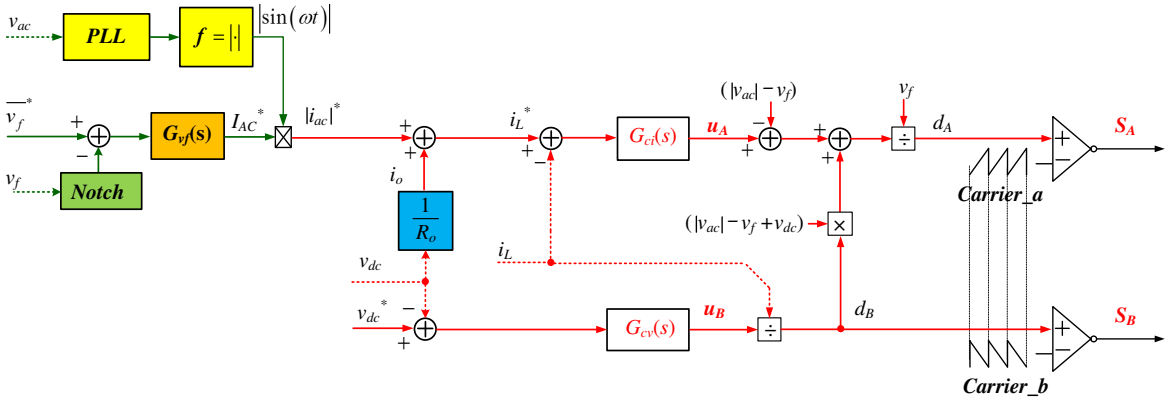

Fig. 6. Control diagrams of the enhanced automatic-power-decoupling-control for the two-switch buck-boost PFC rectifier.

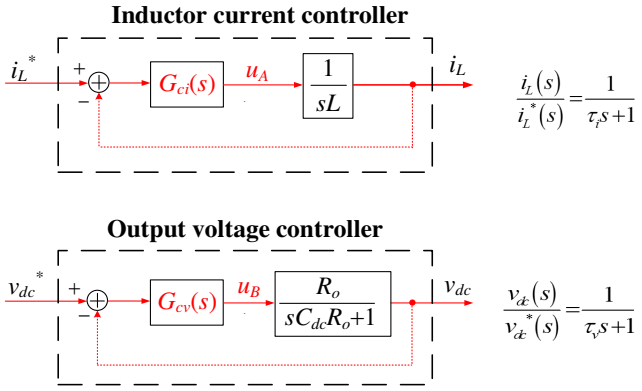

Fig. 7. The simplified control block diagrams of Fig. 6.

Fig. 6 shows the control block diagram for the two-switch buck-boost PFC rectifier based on E-APD control, where i_L and v_{dc} are the direct control outputs. The two control inputs, u_A and u_B, are firstly obtained from two compensators, i.e., $G_{ci}(s)$ and $G_{cv}(s)$ respectively. Based on (23), they are then transformed into the duty cycles d_A and d_B. It should be noticed that three voltage sensors (for measuring v_{ac}, v_f, and v_{dc}) and one current sensor (for measuring i_L) are needed to complete the E-APD control. The number of sensors used is the same as that for the existing DPD and APD control (see Fig. 2 (a) and (b)). A simplified closed-loop diagram of Fig. 6 can be depicted in Fig. 7 with reference to the system model of (21).

Let

$$G_{cv}(s)=\frac{k_{pv}s+k_{iv}}{s}, \tag{27}$$

and set

$$k_{pv}=\frac{C_{dc}}{\tau_v}, \tag{28}$$

$$k_{iv}=\frac{1}{\tau_v R_o}, \tag{29}$$

where τ_v is a time constant. Then, the loop gain of the dc voltage regulation loop is equal to

$$\ell(s)=\frac{1}{\tau_v s}. \tag{30}$$

Then the closed-loop transfer function becomes

$$\frac{v_{dc}(s)}{v_{dc}^{*}(s)} = \frac{1}{\tau_v s + 1}. \tag{31}$$

Equation (31) suggests that, if k_{pv} and k_{iv} in the PI compensator $G_{cv}(s)$ are chosen based on (28) and (29), the response of v_{dc} to v_{dc}^{*} will be based on a first-order transfer function, of which time constant τ_v is a design choice. τ_v should be small enough to enable fast reference tracking but sufficiently large such that $1/\tau_v$, i.e., the bandwidth of the closed-loop control system is relatively smaller than the switching frequency of the single-phase system. For instance, τ_v can be selected as in the range of $2T_s - 10T_s$. It is noticed that no complex *MPR* compensators are needed in the dc voltage control loop. Additionally, the relationship of v_{dc} to u_B is straightforward.

The design of the inductor current compensator $G_{ci}(s)$ follows a similar design procedure.

Let

$$G_{ci}(s) = \frac{L}{\tau_i}, \tag{32}$$

where τ_i is its time constant. Then the loop gain of the inductor current regulation loop has the form of $\ell(s) = 1/(\tau_i s)$, and the closed-loop transfer function becomes

$$\frac{i_L(s)}{i_L^{*}(s)} = \frac{1}{\tau_i s + 1}. \tag{33}$$

Equation (33) indicates that the response of i_L to i_L^{*} again follows a first-order transfer function form whose time constant is τ_i. The design of τ_i is similar to that of τ_v. Again, no *MPR* compensators are used in the inductor current control loop and the response of i_L to u_A is straightforward.

Note that practical circuit parameters such as R_o, C_{dc}, and L might not be precisely known. However, this is not a major issue to the operation of the rectifier, since only the dynamic responses of v_{dc} and i_L are slightly altered. For instance, if the actual inductor has an inductance of L', and the compensator is designed from (32) assuming an inductance of L, then following Fig. 7, one can easily conclude that the equivalent time constant $\tau_i' = (L'/L)\tau_i$. It implies that the minimum bandwidth of the i_L loop is 0.9 times of the original design

assuming an inductance tolerance of 10%. Therefore, the inductor current loop is still fast enough for tracking a relatively slow current reference as indicated by (17).

IV. Simulation and Experiments

A. *Simulation Verification*

Simulation studies are conducted on the two-switch buck-boost PFC rectifier using PSIM. The detailed circuit and control parameters of the rectifier are listed in Table I (where the E-APD compensators are designed based on R_o=100 Ω, while the compensators for DPD and APD control are manually tuned to achieve similar steady-state performance to that with E-APD control). A slight modification is made in the simulation for the reference generation of i_L (as shown in Fig. 8), where direct feedforward of i_{dc} is adopted, as opposed to the method described in Fig. 6. The feedforward term allows a more thorough comparison of the three control methods under load-change scenarios. The performance of the E-APD compensators, which are designed based on a fixed resistive load of R_o, can also be examined.

Table I. Key Simulation and Experiment Parameters.

Parameters	**Values**	**Parameters**	**Values**
Rated power P_o	100 W	Line frequency	60 Hz
RMS AC voltage	110 V	EMI filter cut-off frequency	1.2 kHz
dc output voltage v_{dc}	30 − 100 V	Switching frequency T_s	25 kHz
Output capacitor C_{dc}	10 μF/ 150 V	Inductor L	2.5 mH
Power-buffering capacitor C_f	20 μF/ 450 V		(500V film capacitor)
Diode bridge	UF5404-E3/54 (Vishay Semiconductor)		V_{RRM} : 400 V, I_F : 3 A V_F : 1.0 V, T_{rr} = 50 ns
Diode D_A	SCS206AGC (Rohm Semiconductor)		V_{RRM} : 650 V, I_F : 6 A V_F : 1.35 V, T_{rr} = 0 ns
S_A and S_B	AOT20S60L (Alpha & Omega Semiconductor Inc.)		V_{DS} : 600 V, $R_{DS(ON)}$: 0.199 Ω T_r : 32 ns, T_f : 30 ns

Main Control Parameters	
DPD control	$G_{rv}(s) = 1 + \frac{80}{s^2 + (2\times\pi\times120)^2}$
	$G_{cf}(s) = 0.1 + \frac{18}{s^2 + (2\times\pi\times120)^2}$
APD control	$G_{cv}(s) = 0.05 + \frac{0.5}{s} + \frac{18}{s^2 + (2\times\pi\times120)^2}$
E-APD control	$\tau_i = 2\ T_s = 80\ \mu$s
	$\tau_v = 10\ T_s = 400\ \mu$s

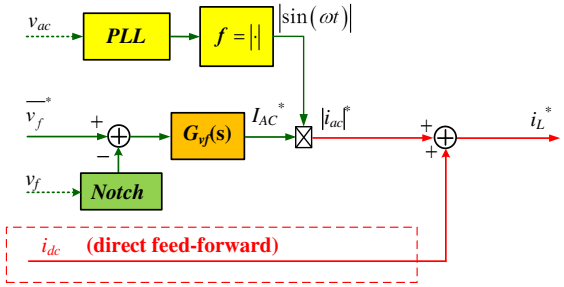

Fig. 8. Generation of the inductor current reference i_L^* with direct i_{dc} feedforward.

The steady-state performance of the rectifier with DPD, APD, and E-APD control are illustrated in Fig. 9 (a)–(c), respectively. In the simulation, v_{ac} is initially sinusoidal at t=0 s, and the load is fixed at R_o. As the voltage waveforms of commercial power lines are often clipped, to test the performance of the rectifier under this condition, the peak of v_{ac} is clipped at t=0.1 s with a crest factor of 1.2. At t=0.2 s, v_{ac} is reverted back to a sinusoidal waveform, but the load is augmented with an additional ac sink (pulsating at 40 Hz with an amplitude of 0.2 A). Based on the simulation results, it can be observed that the three control methods achieve similar steady-state performance before t=0.2 s (in terms of the THD of i_{ac} and the output voltage ripple Δv_{dc}), despite the change of the line voltage profile. Theses are expected results since the system disturbances, including the background harmonics in v_{ac} and the varying ripple-port voltage v_f, are ac components oscillating at multiples of the line frequency. The use of MPR compensators ensures accurate reference generation at the ripple-port for the DPD control, and precise reference tracking for the DPD and APD control. Meanwhile, the E-APD control achieves similar performance due to its inherent disturbance rejection capability. Nonetheless, when the system disturbance is *not* oscillating at multiples of the line frequency (i.e., after t=0.2 s), v_{dc} exhibits significant voltage fluctuation (Δv_{dc}=30.4V) with DPD control and the system performance becomes poor. The reason is that MPR compensator is less effective for reference generation at the ripple port to compensate the random disturbance. In contrast, the system performance with APD control (without the need for reference generation at the ripple port) and E-APD control are much better (Δv_{dc}=6.69 V and Δv_{dc}=4.93 V, respectively) and are comparable to those before t=0.2 s. The results clearly demonstrate the robustness of the APD control over the conventional DPD control approach. A closer

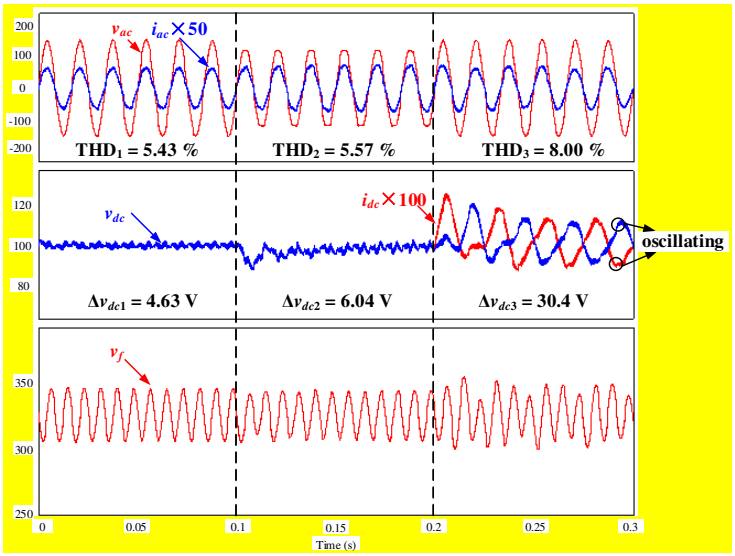
v_{ac}
$i_{ac}\times 50$
$\mathrm{THD}_1 = 5.43\ \%$
$\mathrm{THD}_2 = 5.57\ \%$
$\mathrm{THD}_3 = 8.00\ \%$
v_{dc}
$i_{dc}\times 100$
oscillating
$\Delta v_{dc1} = 4.63$ V
$\Delta v_{dc2} = 6.04$ V
$\Delta v_{dc3} = 30.4$ V
v_f
Time (s)

(a)

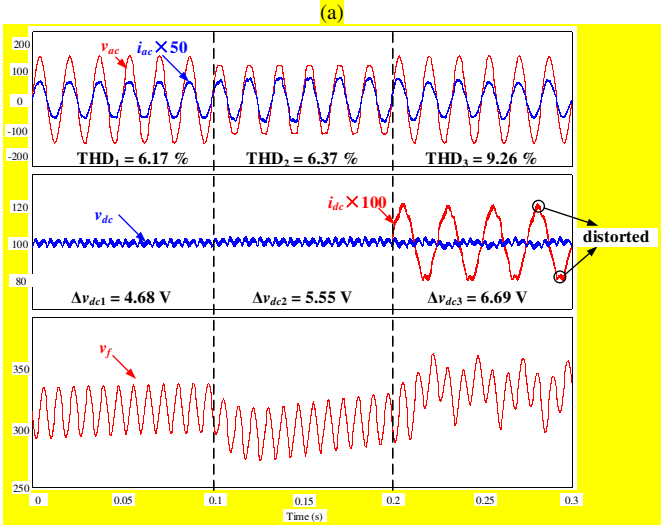
v_{ac}
$i_{ac}\times 50$
$\mathrm{THD}_1 = 6.17\ \%$
$\mathrm{THD}_2 = 6.37\ \%$
$\mathrm{THD}_3 = 9.26\ \%$
v_{dc}
$i_{dc}\times 100$
distorted
$\Delta v_{dc1} = 4.68$ V
$\Delta v_{dc2} = 5.55$ V
$\Delta v_{dc3} = 6.69$ V
v_f
Time (s)

(b)

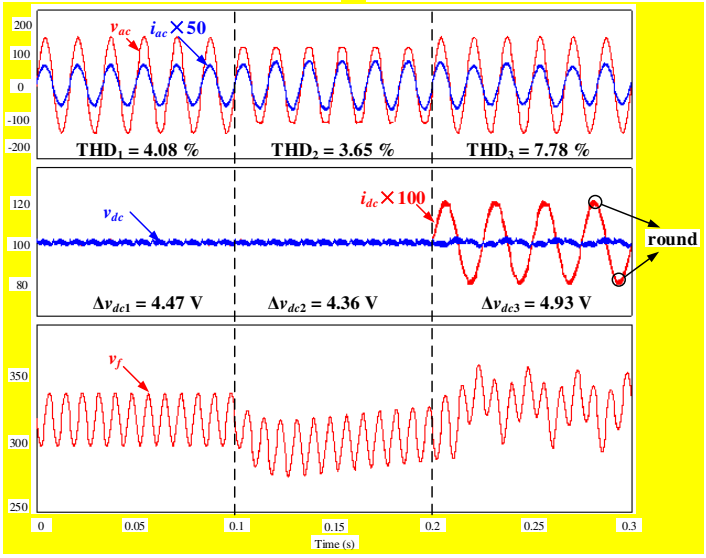
v_{ac}
$i_{ac}\times 50$
$\mathrm{THD}_1 = 4.08\ \%$
$\mathrm{THD}_2 = 3.65\ \%$
$\mathrm{THD}_3 = 7.78\ \%$
v_{dc}
$i_{dc}\times 100$
round
$\Delta v_{dc1} = 4.47$ V
$\Delta v_{dc2} = 4.36$ V
$\Delta v_{dc3} = 4.93$ V
v_f
Time (s)

(c)

Fig. 9. Simulated operating waveforms of the two-switch buck-boost PFC rectifier under periodic input/output disturbances with (a) DPD control, (b) APD control, and (c) E-APD control.

examination of i_{dc} shows that the E-APD control achieves a slightly better performance than the APD control (the ac component in i_{dc} is slightly distorted in Fig. 9 (b) while it is almost sinusoidal in Fig. 9 (c)). This is because the use of MPR compensators may not achieve satisfied reference tracking performance in the presence of a random disturbance. Recall that the compensators for the E-APD control are designed based on a fixed R_o. Fig. 9 (c) confirms that the performance of the rectifier with E-APD control is not degraded even with a varying load.

Next, the dynamic response of the rectifier is examined with the dc voltage reference being step changed between 100 V and 43 V. At a load of 100 Ω, the output power is changed between 100% (100 W) and 20% (20 W). It can be seen from Fig. 10 (a) and (b) that the use of DPD and APD control leads to a substantially delayed and disturbed step response of v_{dc}. The reason is that a step change of the output power causes a step-ripple-power disturbance. Precise reference generation at the ripple-port and accurate reference tracking with MPR compensators become more challenging as compared to those at the steady state. In contrast, with the proposed E-APD control, v_{dc} follows a first-order transfer function with a settling time of around 2 ms, i.e., $5\tau_v$. This is expected with reference to the design method described in III-B. The buffering of the step-ripple-power disturbance is reflected by the sudden overshoot/undershoot of v_f right after the step-change instant at t=0.1 s and at t=0.2 s, respectively.

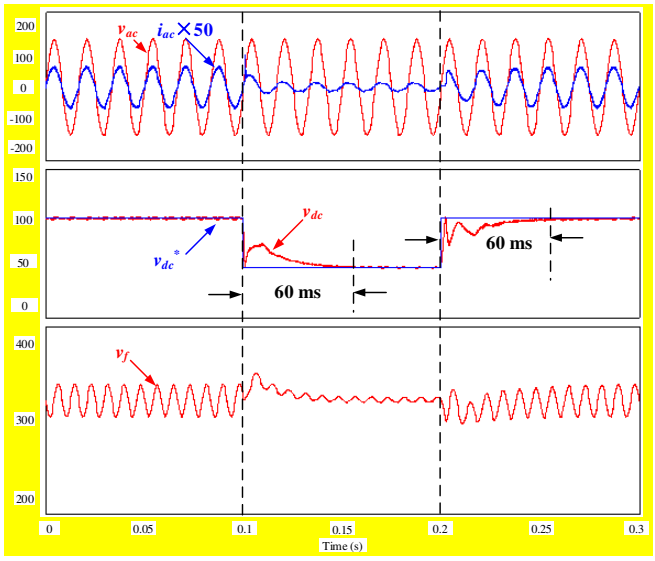
v_{ac}
$i_{ac}\times 50$
v_{dc}
v_{dc}^*
60 ms
60 ms
v_f
Time (s)

(a)

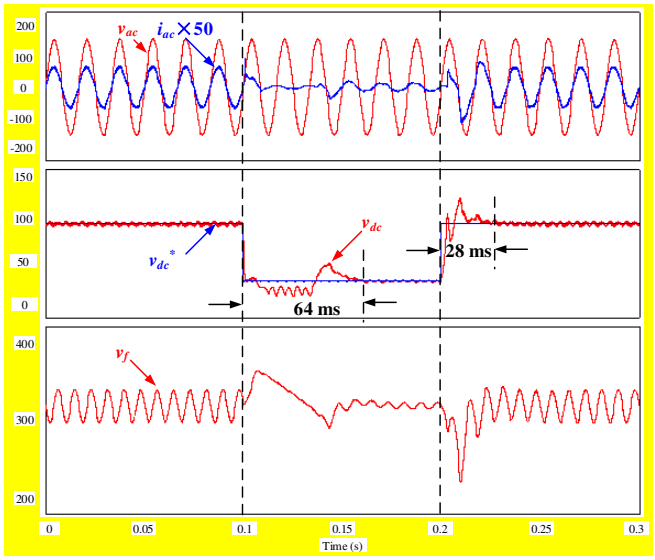
v_{ac}
$i_{ac}\times 50$
v_{dc}
v_{dc}^*
28 ms
64 ms
v_f
Time (s)

(b)

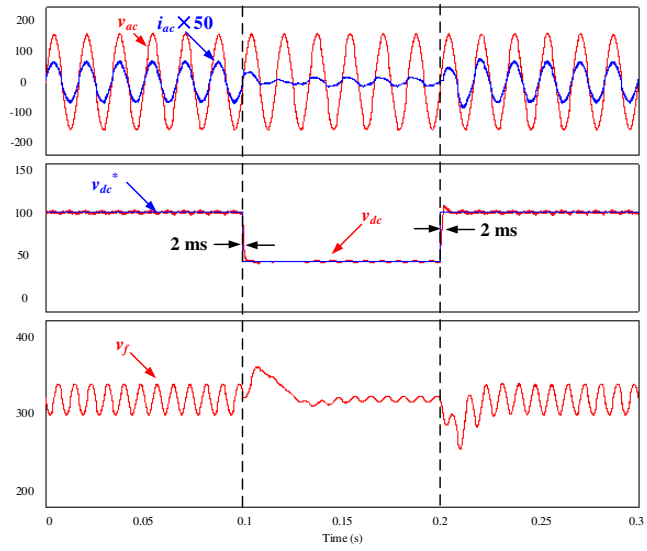
v_{ac}
$i_{ac}\times 50$
v_{dc}^*
v_{dc}
2 ms
2 ms
v_f
Time (s)

(c)

Fig. 10. Simulated operating waveforms of the two-switch buck-boost PFC rectifier with a step change of the dc voltage reference with (a) DPD control, (b) APD control, and (c) E-APD control.

B. Experimental Verification

Experiments are also conducted on a two-switch buck-boost PFC rectifier prototype with the proposed E-APD control. The reference of i_L is generated based on Fig. 6. A fixed resistive load R_o is used to proof the concept of the proposed E-APD control, which is implemented by a low-cost DSP microcontroller (Model No.: F28069). The key parameters of the system are also listed in Table I. A KIKUSUI PCR1000LE ac power supply is used to emulate the ac grid with a minimum crest factor of 1.2.

Fig. 11 illustrates the steady-state waveforms of the rectifier supplied by a pure sinusoidal ac voltage source. It can be seen that i_{ac} is sinusoidal and in phase with v_{ac}. Meanwhile, v_{dc} is precisely regulated at 100 V with a peak-to-peak voltage ripple of merely 5 V (i.e., 5% of v_{dc}). Additionally, v_f is pulsating at double-line frequency indicating that a periodic ripple power is being buffered. These steady-state waveforms are comparable to those shown in Fig. 9(c) before 0.1 s. The measured THD of the input current is 3.6%, and the measured PF is 0.99.

The peak of v_{ac} is then clipped with a crest factor of 1.2. v_{ac} hence contains rich line-frequency-harmonic components. As shown in Fig. 12, v_{dc} is still tightly regulated with the same ripple-voltage performance. The slight distortion in i_{ac} is due to the disturbance in i_L^* generation since the notch filter (see Fig. 6) is incapable of removing all the high-order components in v_f caused by the clipped v_{ac}. The measured THD is 18.6% and the PF is 0.94. The performance of i_{ac} may be improved with a more accurate dc-extraction algorithm, such as employing a moving average filter or the method proposed in [22]. Another observation from Fig. 12 is that v_f is less symmetrical as compared to that in Fig. 11. The reason is that C_f needs to buffer high-frequency ripple power components that are induced by the input voltage harmonics, besides the double-line frequency ripple power indicated by (5).

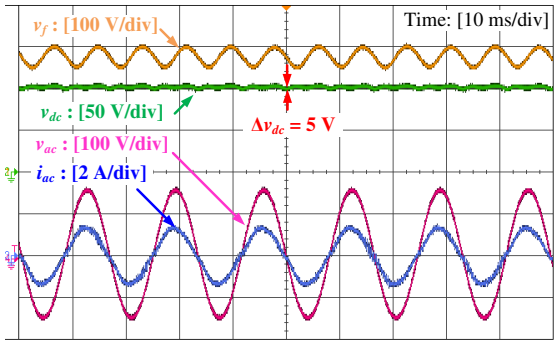

Fig. 11. Steady-state operating waveforms of the two-switch buck-boost PFC rectifier with sinusoidal ac voltage input (crest factor=1.414).

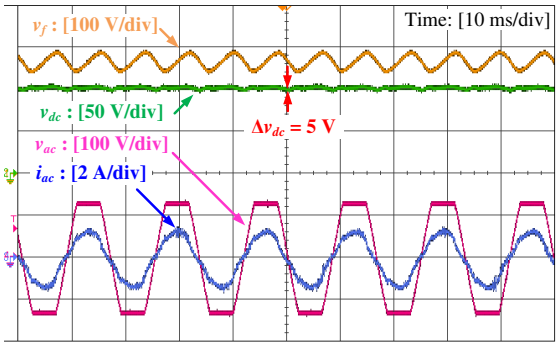

Fig. 12. Steady-state operating waveforms of the two-switch buck-boost PFC rectifier with peak-clipped ac voltage input (crest factor=1.2).

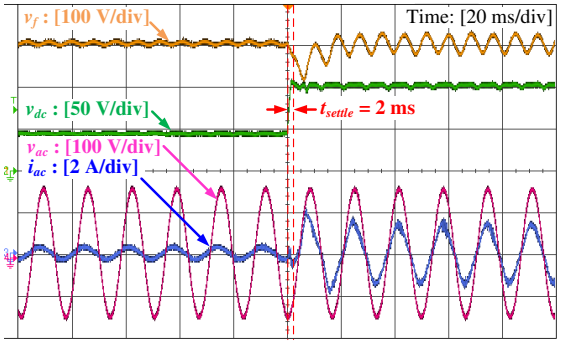

(a)

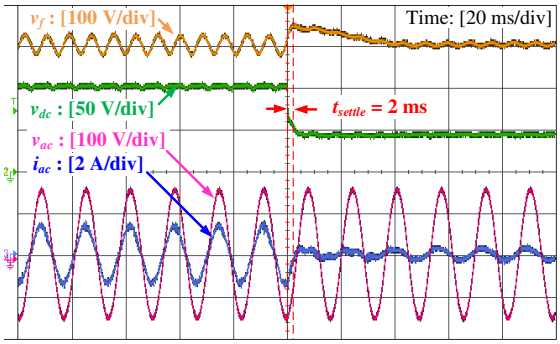

(b)

Fig. 13. Transient waveforms of the two-switch buck-boost PFC rectifier with v_{dc}^* (a) steps up from 43 V to 100 V and (b) steps down from 100 V to 43 V.

To examine the dynamic performance of the E-APD control, transient tests of input/output voltage change are performed. Fig. 13 illustrates the time response of the rectifier to a step change of v_{dc}^* (between 100 V to 43 V). The waveforms are comparable to those shown in Fig. 10 (c), where v_{dc} reaches its steady state within 2 ms ($5\tau_v$). Fig. 14 illustrates the dynamic behavior of the rectifier in the event of a sudden ac voltage sag/swell (of 20% of the rated value) and voltage clipping. Due to the automatic-power-decoupling capability and the robustness of the E-APD control, v_{dc} is almost immune to the line voltage variation in all three cases.

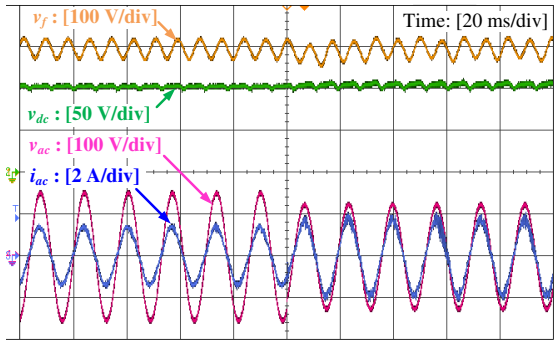

(a)

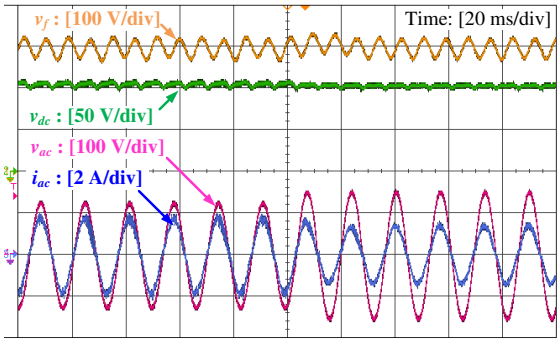

(b)

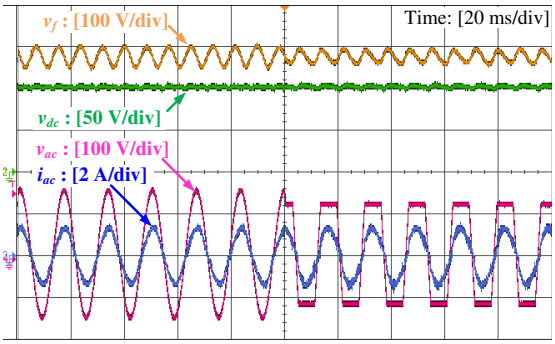

(c)

Fig. 14. Dynamic waveforms of the two-switch buck-boost PFC rectifier with input voltage v_{ac} (a) sag (20% of v_{ac_rated}) (b) swell (20% of v_{ac_rated}), and (c) peak clipped (crest factor=1.2).

The E-APD control can also improve the system's start-up and shut-down performances. Fig. 15(a) shows the waveforms of the rectifier, which is directly started up from 0 to the rated power without any soft-start process. The small reactive current of i_{ac} before the start-up is introduced by the front-end EMI filter. Due to the fast time response of rectifier, v_{dc} quickly settles to the steady-state value within one line cycle. The initial undershoot/overshoot in v_{dc} is caused by the relatively low voltage level of v_f during the start-up since (18) must be satisfied before the rectifier can operate normally. In contrast, the start-up waveforms with DPD control is rarely discussed in the prior arts. In [19], the start-up performance with APD control is simulated for the two-switch buck-boost rectifier. It takes more than 9 line cycles to reach the steady state. In [23], another single-phase system with APD control takes about 15 line cycles to complete the start-up process, during which significant voltage variation of v_{dc} are observed.

Finally, the shut-down waveforms of the rectifier are illustrated in Fig. 15 (b). The rectifier is shown to be capable of providing additional power hold-up function (i.e., v_{dc} remains regulated after the input voltage is turned off) for approximately 5.6 ms (34% of the line cycle). The continued regulation of v_{dc} is feasible because the dynamics of v_{dc} is still governed by (21) and can still be actively controlled by u_A. The energy stored in C_f is then used to supply the required load power. Once v_f is discharged below 100 V, v_{dc} cannot remain at 100 V and will drop together with v_f, since (18) must be satisfied (where $|v_{ac}|$=0). Clearly, the holdup time of the rectifier is simultaneously dependent on the energy stored in C_f at the shut-down instant, p_{dc}, and v_{dc}. The minimum holdup energy E_{hd_min} provided by C_f can be calculated as

$$E_{hd\_\min} = \frac{1}{2} C_f \left({v_{f\_\min}}^2 - {v_{dc}}^2 \right) = \int_0^{t_{hd}} p_{dc}(t)\, dt, \tag{34}$$

where $v_{f\_\min}$ is the minimum voltage of v_f before the system shuts down, and t_{hd} is the holdup time. C_f can then be determined based on the loading condition and the required hold-up time requirement. Such an active-power-holdup function empowered by the E-APD control is interesting as compared to conventional passive

power-holdup solutions (i.e., simply using a large capacitor to hold up v_{dc}) since the required energy storage can be reduced.

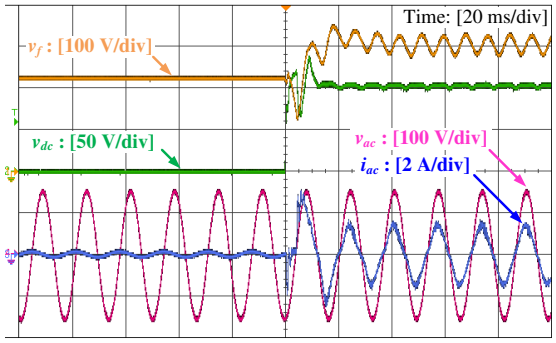

(a)

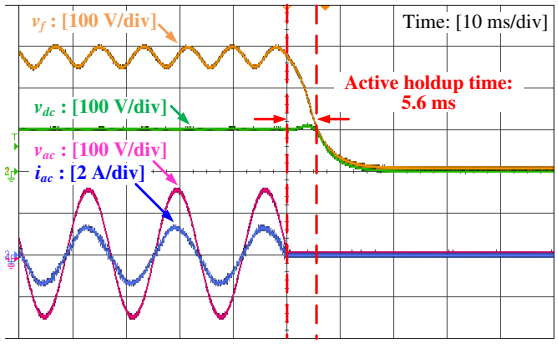

(b)

Fig. 15. (a) Start-up and (b) shut-down waveforms of the two-switch buck-boost PFC rectifier.

V. Conclusions

This paper firstly presents a systematic overview of the existing control methods for a single-phase ac-to-dc power converter with active power decoupling function. It is shown that the recently proposed APD control possesses a simpler control structure and improved robustness of the closed-loop system toward disturbance as compared to that with the conventional DPD control. However, it is found that both APD and DPD control suffer from high control/computational complexity and that they give poor dynamic control performances and robustness against load and input variations. An enhanced APD (E-APD) control is then proposed in this paper and applied to a recently proposed two-switch buck-boost PFC rectifier for illustration. Both simulation and experiment results show that with only simple compensators, the rectifier easily achieves superior dynamic responses and high robustness against input/load/reference variation. Additionally, the

design of the compensator is straightforward and is easily extendable to other single-phase systems that have an active power-decoupling function.

REFERENCES

[1] P. T. Krein, R. S. Balog, and M. Mirjafari, "Minimum energy and capacitance requirements for single-phase inverters and rectifiers using a ripple port," *IEEE Trans. Power Electron.*, vol. 27, no. 11, pp. 4690–4698, Nov. 2012.

[2] R. Wang, F. Wang, D. Boroyevich, R. Burgos, R. Lai, P. Ning, and K. Rajashekara, "A high power density single-phase PWM rectifier with active ripple energy storage," *IEEE Trans. Power Electron.*, vol. 26, no. 5, pp. 1430–1443, May 2011.

[3] H. Hu, S. Harb, N. Kutkut, I. Batarseh, and Z. J. Shen, "A review of power decoupling techniques for microinverters with three different decoupling capacitor locations in PV systems," *IEEE Trans. Power Electron.*, vol. 28, no. 6, pp. 2711–2726, Jun. 2013.

[4] J. W. Kolar, U. Drofenik, J. Biela, M. L. Heldwein, H. Ertl, T. Friedli, and S. D. Round, "PWM Converter power density barriers," in *2007 Power Conversion Conference - Nagoya*, 2007, p. P–9–P–29.

[5] H. Wang, M. Liserre, and F. Blaabjerg, "Toward reliable power electronics: challenges, design tools, and opportunities," *IEEE Ind. Electron. Mag.*, vol. 7, no. 2, pp. 17–26, Jun. 2013.

[6] T. H. Nguyen and D.-C. Lee, "Deterioration monitoring of DC-link capacitors in AC machine drives by current injection," *IEEE Trans. Power Electron.*, vol. 30, no. 3, pp. 1126–1130, Mar. 2015.

[7] S. Wang, X. Ruan, K. Yao, S.-C. Tan, Y. Yang, and Z. Ye, "A flicker-free electrolytic capacitor-less AC–DC LED driver," *IEEE Trans. Power Electron.*, vol. 27, no. 11, pp. 4540–4548, Nov. 2012.

[8] T. Shimizu, T. Fujita, G. Kimura, and J. Hirose, "A unity power factor PWM rectifier with DC ripple compensation," *IEEE Trans. Ind. Electron.*, vol. 44, no. 4, pp. 447–455, 1997.

[9] H. Li, K. Zhang, H. Zhao, S. Fan, and J. Xiong, "Active power decoupling for high-power single-phase PWM rectifiers," *IEEE Trans. Power Electron.*, vol. 28, no. 3, pp. 1308–1319, Mar. 2013.

[10] M. Su, P. Pan, X. Long, Y. Sun, and J. Yang, "An active power-decoupling method for single-phase AC–DC converters," *IEEE Trans. Ind. Informatics*, vol. 10, no. 1, pp. 461–468, Feb. 2014.

[11] Y. Tang and F. Blaabjerg, "A component-minimized single-phase active power decoupling circuit with reduced current stress to semiconductor switches," *IEEE Trans. Power Electron.*, vol. 30, no. 6, pp. 2905–2910, Jun. 2015.

[12] W. Cai, L. Jiang, B. Liu, S. Duan, and C. Zou, "A power decoupling method based on four-switch three-port DC/DC/AC converter in DC microgrid," *IEEE Trans. Ind. Appl.*, vol. 51, no. 1, pp. 336–343, Jan. 2015.

[13] W. Qi, H. Wang, X. Tan, G. Wang, and K. D. T. Ngo, "A novel active power decoupling single-phase PWM rectifier topology," in *IEEE Applied Power Electronics Conference and Exposition*, 2014, pp. 89–95.

[14] Y. Sun, Y. Liu, M. Su, W. Xiong, and J. Yang, "Review of active power decoupling topologies in single-phase systems," *IEEE Trans. Power Electron.*, pp. 1–1, 2015.

[15] Y. Sun, Y. Liu, M. Su, X. Li, and J. Yang, "Active power decoupling method for single-phase current-source rectifier with no additional active switches," *IEEE Trans. Power Electron.*, vol. 31, no. 8, pp. 5644–5654, Aug. 2016.

[16] S. Li, G.-R. Zhu, S.-C. Tan, and S. Y. R. Hui, "Direct AC/DC rectifier with mitigated low-frequency ripple through inductor-current waveform control," *IEEE Trans. Power Electron.*, vol. 30, no. 8, pp. 4336–4348, Aug. 2015.

[17] S. Li, W. Qi, S.-C. Tan, and S. Y. R. Hui, "Integration of an active filter and a single-phase AC/DC converter with reduced capacitance requirement and component count," *IEEE Trans. Power Electron.*, vol. 31, no. 6, pp. 4121–4137, Jun. 2016.

[18] Y. Tang, Z. Qin, F. Blaabjerg, and P. C. Loh, "A dual voltage control strategy for single-phase PWM converters with power decoupling function," *IEEE Trans. Power Electron.*, vol. PP, no. 99, pp. 1–1, 2014.

[19] W. long Qi, S. N. Li, S. C. Tan, and S. Y. R. Y. R. Hui, "A two-switch buck-boost PFC rectifier with automatic AC power decoupling capability," in *IEEE Energy Conversion Congress and Exposition*, 2016.

[20] Q.-C. Zhong and W.-L. Ming, "A θ-Converter that reduces common mode currents, output voltage ripples and total capacitance required," *IEEE Trans. Power Electron.*, pp. 1–1, 2016.

[21] Y. Tang, Z. Qin, F. Blaabjerg, and P. C. Loh, "A dual voltage control strategy for single-phase PWM converters with power decoupling function," in *2014 IEEE Energy Conversion Congress and Exposition (ECCE)*, 2014, pp. 4102–4109.

[22] M. Pahlevani and P. Jain, "A fast DC-bus voltage controller for bidirectional single-phase AC/DC converters," *IEEE Trans. Power Electron.*, vol. 30, no. 8, pp. 4536–4547, Aug. 2015.

[23] W.-L. Ming and Q.-C. Zhong, "Current-stress reduction for the neutral inductor of θ-converters," *IEEE Trans. Power Electron.*, pp. 1–1, 2016.